Design, manufacturing and testing of a compact thermoacoustic refrigerator

Islam Ramadan, Hélène Bailliet, Gaëlle Poignand, David Gardner

Design, manufacturing and testing of a compact thermoacoustic refrigerator

Islam A. Ramadan[£], Hélène Bailliet[*],

Institut Pprime, CNRS - Université de Poitiers-ENSMA, Département Fluides-Thermique-Combustion, ENSIP, 6 rue Marcel Doré Bât. B17-BP 633, 86022 Poitiers Cedex, France.

Gaëlle Poignand,

Laboratoire d'Acoustique de l'Université du Mans (LAUM), UMR 6613, Institut d'Acoustique - Graduate School (IA-GS), CNRS, Le Mans Université, France

David Gardner

Los Alamos National Laboratory (retired)

15709 81st Avenue, Kenmore, WA 98028

(First submission date: June 23, 2020)

Running title: A Compact Thermoacoustic Refrigerator

---

[*] helene.bailliet@univ-poitiers.fr; Corresponding author

[£] Now at : Université de Technologie de Compiègne, CNRS, Roberval (Mechanics energy and electricity), Centre de recherche Royallieu - CS 60 319 - 60 203 Compiègne Cedex

1

Abstract

Thermoacoustic refrigeration technology is a green alternative for the conventional refrigeration system in vehicles. The former uses environmentally friendly inert gases whereas the latter uses chemical refrigerants that can have severe impacts on the environment. In order to apply thermoacoustic technology in the automobile industry, the size and the weight of plausible thermoacoustic refrigerators should be decreased.

The design of a new compact thermoacoustic refrigerator is described in this study. This thermoacoustic refrigerator uses two electroacoustic components and one thermoacoustic core. The technical details of design, fabrication, and testing processes are presented. A methodology for thermal design of the heat exchangers is proposed and validated by measurements. The effects of different parameters, such as the driver piston displacement amplitude, the phase shift between the voltage signals applied to the electroacoustic components, and the cold side temperature on the performance indices of the refrigerator are investigated.

The performance of the prototype is compared with the performance calculated by the DeltaEC design model. The overall agreement between the calculated and the measured performance parameters is fair, but further insight into the temperature distributions reveals that non-linear effects yield discrepancies between the model and the experiments. A preliminary discussion of the origin of these discrepancies is proposed.

Keywords: Thermoacoustic; Refrigerator; Thermal design; Design and manufacturing.

1. INTRODUCTION

Chemical refrigerants (such as CFCs and HFCs) used for vapor-compression refrigeration in air conditioning systems are recognized as a source of pollution from a vehicle. Also, cooling systems cause significant increase in power consumption and reduce the overall efficiency of the vehicle. The automotive industry therefore devotes efforts to downsizing thermal needs (isolation, optimized diffusion ...) but also to improve the performance of the refrigeration loop, especially the efficiency of high performance heat pumps. For this purpose, alternative "green" technologies are being considered (e.g. [1], [2], [3], [4], [5]). Thermoacoustic cooling devices are systems that offer potentially attractive alternatives [6], especially with the rapid development of hybrid and electric vehicles. Thermoacoustic refrigerators use acoustic energy to pump heat from a cold source to a hot sink. They include an acoustic resonator coupled to an acoustic source and are typically filled with an inert gas as working fluid. Inside the gas column is inserted the thermoacoustic core (TAC), that consists of an open cell porous medium referred to as stack or regenerator, sandwiched between two heat exchangers which are responsible for the heat exchange processes between the working gas and the thermal reservoirs.

Thermoacoustic technology is characterized by relatively simple construction and potentially low maintenance cost. However, to date, very few thermoacoustic refrigeration systems [6] , [7], [8], [9] have been investigated for adaptation to the automobile. One of the main reasons, among others, is that the automotive applications are associated with strict restrictions on weight, size, and cost. An innovative device needs to be no larger or heavier than the current Heating, Ventilation Air Conditioning (HVAC) systems, yet ensuring comparable performance.

In usual thermoacoustic devices, the size is driven by resonance conditions yielding metric devices with working frequencies of the order of 10^2 Hz. Such devices do not fit size and weight

criteria for automotive applications. The objective of the present study is to propose a new thermoacoustic refrigerator that is competitive compared to the existing technology in terms of space (the target set for the volume is about 24 liters) and performance (the target set for the performance coefficient COP is about 1.1); the temperature of the air supplied to the passenger compartment of the vehicle has to vary from 5 to 15 degrees.

Since the pioneering works of John Wheatley and Gregory Swift at Los Alamos National Laboratories at the beginning of the 1980's, thermoacoustics has spread over the research world and the research in thermoacoustics is still a topical issue today [10]. The field was very active in the 1990's, with a great deal of fundamental research undertaken. From the 2000's, more applied research devoted to specific applications has appeared such as cryogenics [11], natural gas liquefaction [12], electricity generation [13], domestic refrigeration [14], and thermal management of electronic devices [15]. Thanks to both fundamental and applied research, the performance of thermoacoustic devices has progressed. Twenty-five percent of Carnot coefficient-of-performance was obtained by a thermoacoustic refrigerator driven by an electroacoustic source developed at the Energy Research Center of the Netherlands [16]. This device consists of a 2.9 m half wavelength resonator with a coaxial thermoacoustic core and is driven by an electroacoustic source. In 2015, a multi-stage thermoacoustic cryocooler with a 11 m loop length was developed [17] with a cooling capacity of about 1 kW at liquefied natural gas temperature range. As discussed in the review by Tartibu [18], several other highly efficient travelling wave thermoacoustic devices have been developed in the last decades. The associated refrigerators geometrical configurations consist of single or multiple regenerators connected in series inside a closed-loop tube together with an acoustic source that is either in series with the regenerator(s) inside the loop (e.g. [19] [20]) or coupled to the loop via a side branch (e.g. [14]

4

[21]). Such devices are associated with typical cooling capacities of few hundreds of Watts. Their design is driven by resonance conditions yielding metric devices so that their architecture is not adapted to automotive application. Because many applications are associated with size constraints [22] [23], some compact thermoacoustic devices have already been developed. Among those, the Ben & Jerry's "bellows-bounce" freezer has a 25 cm diameter and a 48 cm length and pumps 120 W at a -20°C load temperature with a 19% of Carnot coefficient-of-performance [24].

In the current work, we used the concept of two-source co-axial compact thermoacoustic refrigerator proposed by Poignand, *et al*. [25], [26] to reach compactness. This concept is based on replacing the resonator historically used to reach high acoustic power and appropriate phase relationship between particle displacement and instantaneous temperature by an effective acoustic impedance provided by a second acoustic source. It follows that the thermoacoustic cavity is fitted with two electroacoustic components working at the same frequency whose amplitudes and phases can be independently tuned for optimizing the performances of the device. Acoustic pressure and particle velocity are therefore no longer linked by quasi-standing wave or quasi-travelling wave conditions as was the case in standing wave devices or travelling wave devices. The working frequency can thus be set so that the wavelength is much greater than the dimensions of the resonator and the compactness of the device is thus significantly improved. This concept of a compact refrigerator has been validated with an academic setup that showed both stack-based and regenerator-based compact devices can reach the same performance as non-compact geometries in terms of temperature difference, heat flux or COP [27]. The purpose of the present work is to develop a compact thermoacoustic device that reach high specific cooling capacity (i.e. the ratio between the cooling capacity and the total volume of the device). This

requirement imposes many challenges, especially in thermal and mechanical design, and fabrication processes.

In Section 2, a description of the device is presented, followed by a detailed description of the thermal and mechanical design of the heat exchangers. Then, the instrumentation and control systems of the device are explained. In Section 3, the results of the experiments are discussed and compared with the numerical predictions. In Section 4, the conclusions are drawn.

2. EXPERIMENTAL APPARATUS

2.1. Description of the device

A photograph of the thermoacoustic refrigerator is shown in Figure 1a; Figure 1b shows a scale drawing that depicts the main components of the refrigerator; Figure 1c shows a cross sectional view of the refrigerator. The system consists of two compartments (the right and the left compartments) filled with a helium-argon mixture (70% He 30% Ar on a volumetric basis) at a static pressure of 40 *bar*. The piston of the acoustic diver separates the two compartments. The gas volume of the right compartment (8 *L*) is double the gas volume of the left compartment (4 *L*).

The right compartment includes the acoustic driver, which is placed in a back cavity. The acoustic driver (Rix Industries, model: 1S241M) has a maximum input electric power of 1600 *W*. The piston of the acoustic driver has a diameter of 108 *mm*, with a maximum displacement amplitude of 10 *mm* (i.e. stroke limits are ±10 *mm*). The seal gap between the piston and the cylinder within which it oscillates is about 30 μm; the moving mass is 4.2 *kg*, the stiffness of the spring is 131 *kN/m*, the coil resistance is 0.7 Ω, and the inductance is 31.7 mH.

Essentially, the left compartment includes the thermoacoustic core (i.e. regenerator and the heat exchangers) and the impedance-control loudspeaker (henceforth, loudspeaker). A cone (initial diameter of 108 mm and final diameter of 164 mm) is used to match between the piston area and the area of the thermoacoustic core. At the end of the cone, the flow is divided into two paths, the central path (that includes the thermoacoustic core) and the peripheral channel (see the zoom view in Figure 1b). The central path consists of a cylinder with inner and outer diameters of 152 *mm* and 156 *mm*, respectively. The peripheral channel (feedback) is an annulus with inner and outer diameters of 156 *mm* and 164 *mm*, respectively. In order to minimize the heat conducted to the peripheral channel from the thermoacoustic core, the inner tube is made of stainless steel that has very low thermal conductivity compared to other metals such as copper or aluminum. During the design stage, the heat conducted through the walls of the inner tube was calculated at the maximum expected temperature difference (between the thermoacoustic core and the peripheral channel) and it was found to be very low (few Watts) compared to the cooling capacity

This feedback loop makes it possible to connect the front of the acoustic driver to the rear of the loudspeaker (Peerless, model: GBS-135F, moving mass: 12.3 *g*, spring stiffness: 1926 *N/m*, coil resistance: 3.3 Ω, coil inductance: 0.21 *mH*), and is a particularity of the device. Accordingly, the loop, together with the relative phase of the input signals at the two electro acoustic components, allows the phase difference between pressure and acoustic displacement at the regenerator to be adjusted.

In order to adjust the relative phase between the acoustic driver and the loudspeaker, a two-channel function generator (TekTronix, model: AFG3022) is used to drive the power amplifiers of both the acoustic driver and the loudspeaker.
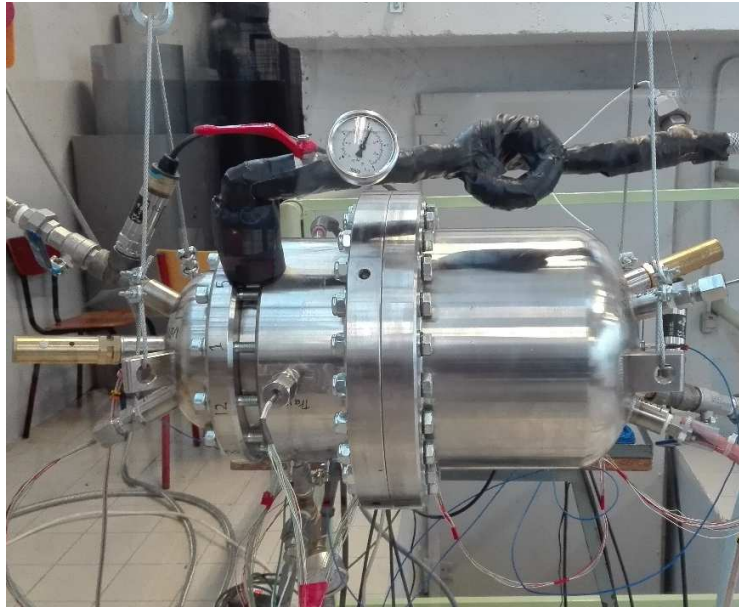
7

Two flow straighteners, made of a 20-mesh stainless steel square-weave screen and a wire diameter of 0.37 *mm*, are placed at both ends of cone to promote uniform flow at the entrance of the thermoacoustic core.

The thermoacoustic core consists of the regenerator, the Ambient Heat Exchanger (AHX) and the Cold Heat Exchanger (CHX). The regenerator is made of hundreds of 214-mesh stainless steel screen discs with a wire diameter of 43 *μm* machined to a diameter of 148 *mm*. The screens are stacked within a thin stainless steel canister that has a length of 39 *mm*. As shown in Figure 1d, nine thermocouples are placed at different axial and radial locations inside the regenerator to measure the temperatures. At each end of the canister, 3 *mm*-thick cross ribs are welded to the canister to keep the screens stacked and to provide the spacing between the regenerator and each of the heat exchangers. The total weight of the screens is measured in order to determine the volumetric porosity (φ) of the regenerator (i.e. the ratio between the gas volume and the total volume of the regenerator). The volumetric porosity (φ) is about 74 % and the hydraulic radius (r_h), the ratio between the cross-sectional area of a screen pore and the pore perimeter, is 30 *μm*. In order to promote intimate contact between the gas and the solid inside the regenerator (i.e. isothermal heat transfer), the hydraulic radius should be smaller than the thermal penetration depth (δ_k), which is defined as follows:

$$\delta_k = \sqrt{k_g/\pi f \rho_g c_g} \tag{1}$$

where, k_g is the thermal conductivity of the gas mixture, f is the frequency of the oscillations, ρ_g is the density of the gas mixture and c_g is the isobaric specific heat of the gas mixture. Under working conditions, wherein the regenerator is supporting a thermal gradient, the thermal penetration depth inside the regenerator varies from 118 to 145 *μm*, and is much larger than the

hydraulic radius of the regenerator. The design and the construction of the heat exchangers are discussed in the following section.

(a)

1: Back cavity of the acoustic driver
2: Acoustic driver
3: Flow straightener
4: Cold Heat Exchanger (CHX)
5: Regenerator
6: Ambient Heat Exchanger (AHX)
7: Loudspeaker
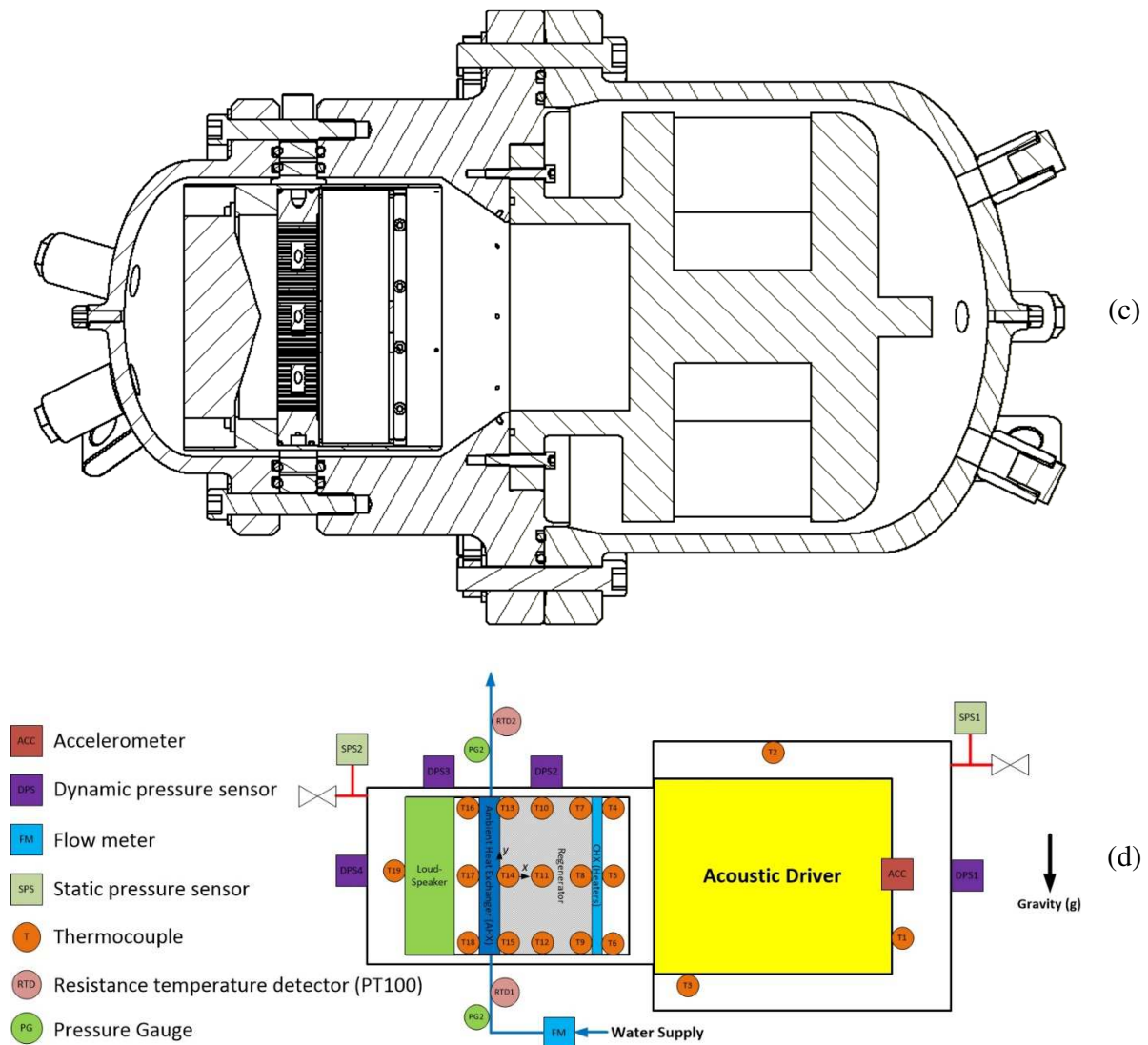8: Peripheral channel (feedback)
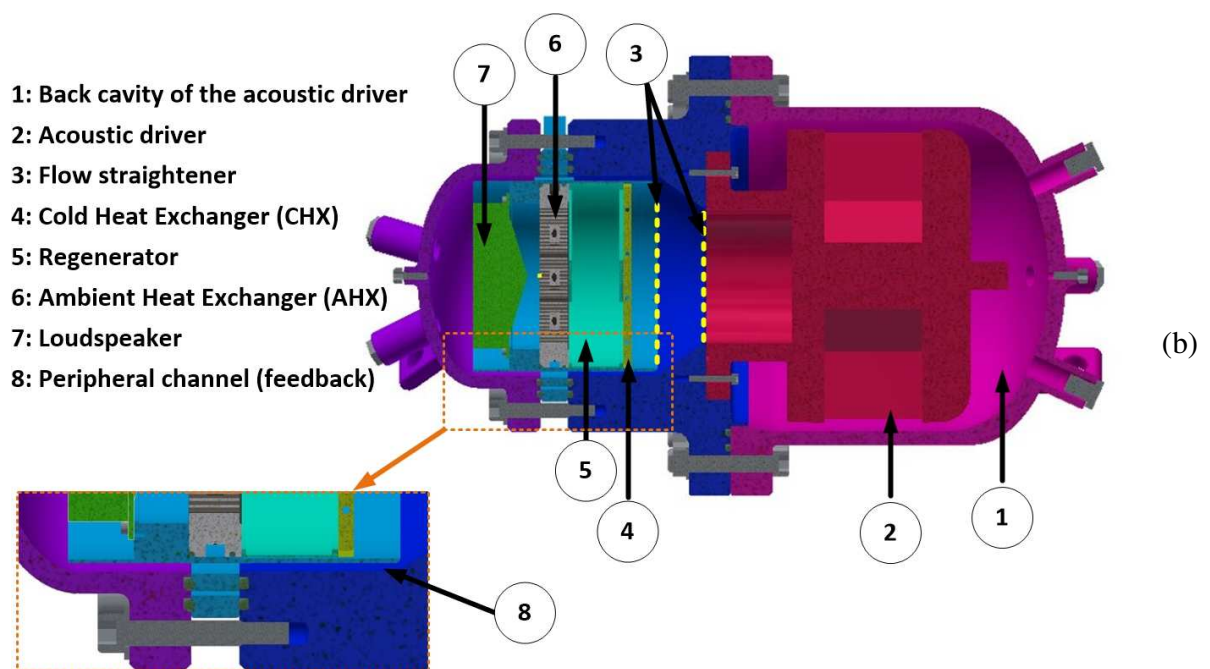
(b)

Figure 1: (a) Photograph of the thermoacoustic refrigerator, (b) Schematic showing the main components of the refrigerator, (c) Cross sectional drawing of the refrigation showing the details of the design, (d) Schematic for the location of the different measurements sensors

2.2. Design of the heat exchangers

Heat exchangers play a vital role in the performance of any thermoacoustic device. Heat exchangers are responsible for removing or adding certain heat quantities to maintain a desired temperature gradient across the regenerator or the stack. The design of heat exchangers for

10

thermoacoustic device has several constraints: the flow is oscillating as opposed to the more common uniform flow direction in heat exchangers. For the design of thermoacoustic device heat exchangers, a common practice is that the length of the heat exchanger should be about two times the acoustic particle displacement amplitude, which usually ranges from several mm to few cm. It follows that the heat exchangers should remove a certain quantity of heat over a small distance; hence the heat transfer surface area should be maximized to achieve this required heat transfer. Also, the porosity of the heat exchanger (i.e. the ratio of gas area to the total area) should be adjusted so that the heat transfer surface area is large but the blockage of the flow should be reasonable to avoid excessive pressure drop across the heat exchanger in the oscillating flow.

In the present study, DeltaEC, a modeling program developed at Los Alamos National Laboratory [28] was used to explore the characteristics of the heat exchangers, namely the amount of heat removed, the length of the exchanger (in the axial direction), and the area and porosity. DeltaEC can also model the heat transfer process between the oscillating gas and the metal of the heat exchanger. However, it cannot describe the heat exchange process between the metal of the heat exchanger and the heat carrier fluid, such as water. The performance of the heat exchange processes on both sides of the heat exchanger is very important because the shortage of heat transfer on one side limits the whole performance of the heat exchanger and thus of the device. In the following subsections, a method for the thermal design of the heat exchangers, which augments the DeltaEC calculation, is proposed.

2.2.1. Design of the Ambient Heat Exchanger (AHX)

The ambient heat exchanger is responsible for extracting the heat transported from the cold section of the refrigerator. The thermal design of the heat exchanger for our device followed an

iterative process: DeltaEC calculations provided the length, area, and porosity of the heat exchangers. We then examine the heat exchanger performance using the thermal calculations presented later in this section. These calculations are based on the Logarithmic Mean Temperature Difference (LMTD) method, and provide, for a given geometry of heat exchanger, the amount of heat transferred from the gas-side thermoacoustic processes to the water-side. If this amount equals the amount of heat calculated by DeltaEC, then the iterative process ends; otherwise the parameters of the heat exchanger (e.g. surface area on gas and (or) water sides) are adjusted until the results of the two calculation (amount of heat extracted obtained by DeltaEC and by the LMTD method) are equal.

As shown in Figure 2, the proposed architecture for the ambient heat exchanger consists of a shell and tube heat exchanger with a diameter of 110 *mm* and length of 23 *mm*. The heat exchanger is made of copper to exploit its high thermal conductivity (k_c). The water is supplied to 5 tubes via a peripheral channel that has a rectangular cross section (see the yellow dashed lines in Figure 2b). The heat exchanger is oriented radially with respect to the water inlet (see Figure 2b) to increase the path length of the water inside the heat exchanger and hence achieve better heat exchange between the water and the metal of the AHX.

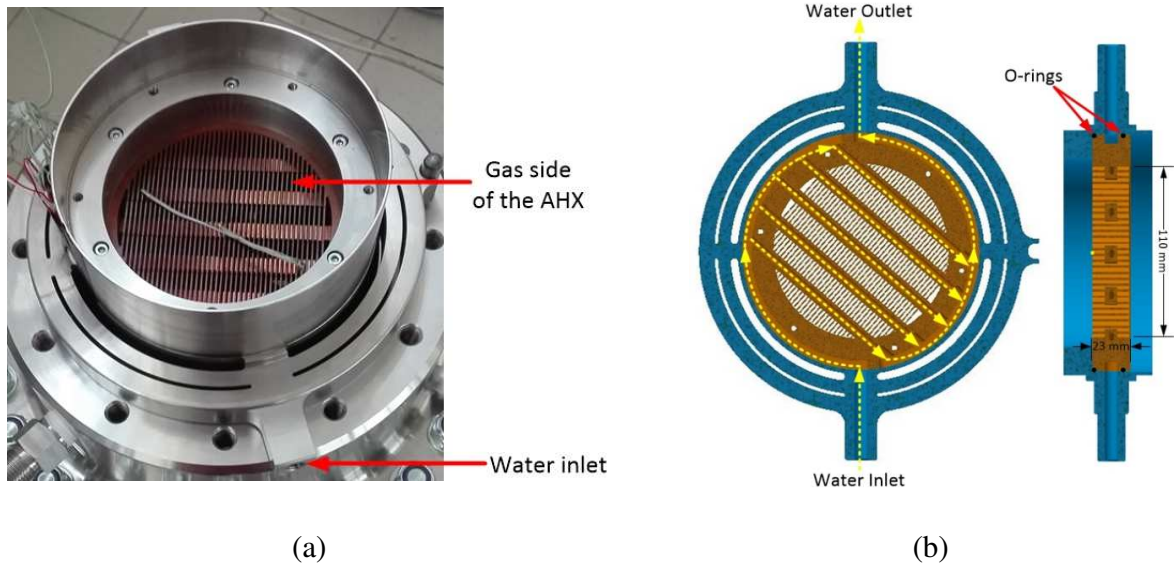<center>(a)   (b)</center>

Figure 2: (a) Photograph for the ambient heat exchanger and (b) Schematic showing the internal design of the ambient heat exchanger

In order to increase the heat transfer surface area on the gas side, electric discharge machining technology was used to form the fins, which are exposed to the oscillating gas. Two O-rings are added on the circumference of the heat exchanger to prevent gas leaks to the water circuit.

Due to the lack of research focusing on the heat transfer associated with oscillating flows, the quasi-steady approach is used and we can profit from the vast available knowledge in the field of heat transfer in steady flow. Accordingly, it is assumed that the gas flow passing through the heat exchangers is a steady flow that has a flow rate equals to the root-mean-square value of the oscillating flow rate.

In order to calculate the logarithmic mean temperature difference, we should determine the gas and water temperatures (T_{g-in}), (T_{g-out}), (T_{w-in}), (T_{w-out}), respectively, at the interface between the AHX and the regenerator, at the exit of the AHX, at the inlet of the AHX water tubes, and at their outlet. The DeltaEC model provides the heat rate $(\dot{Q}_p)$ (the maximum expected

<center>13</center>

heat rate is about 500 W) the gas temperature (T_{g-out}), and the amplitude of the gas volume flow

rate ($\dot{V}_g$). The gas temperature (T_{g-in}) is then estimated using

$$T_{g-in} = T_{g-out} + \frac{\sqrt{2}\dot{Q}_p}{\rho_g \dot{V}_g C_g} \tag{2}$$

On the water-side, the inlet water flow rate ($\dot{m}_w$) and temperature (T_{w-in}) are given by

measurements. The outlet water temperature (T_{w-out}) can be estimated using

$$T_{w-out} = T_{w-in} + \frac{\dot{Q}_p}{\dot{m}_w * C_w} \tag{3}$$

where C_w is the specific heat of the water at the average temperature. In the previous equations,

it is assumed that the heat quantity carried by the gas is entirely transferred to the water stream

with no heat losses. This assumption has been verified experimentally, and will be discussed

later in this section. If a certain amount of heat was not transferred to the water stream, then the

gas temperature on the axially down-steam side of the AHX would increase during the

experiment. This temperature (T17, see Figure 1d) was monitored during the experiments. Under

the steady-state operation, it was observed that the temperature value of T17 is constant, which

indicates that the assumption that all the heat carried by the gas is transferred to the water stream

is a plausible assumption.

These values of the gas and water temperatures are used to calculate the logarithmic mean

temperature difference [29]

$$DT_m = F_t * \frac{(T_{g-in}-T_{w-out})-(T_{g-out}-T_{w-in})}{\ln\left(\frac{T_{g-in}-T_{w-out}}{T_{g-out}-T_{w-in}}\right)} \quad . \tag{4}$$

For the current configuration, the value of the coefficient (F_t) is estimated to be 0.88 [30].

The next step is to calculate the actual heat rate ($\dot{Q}_{AHX}$) removed from one fluid and delivered to another through the metals of a heat exchanger,

$$\dot{Q}_{AHX} = U_w * A_w * DT_m = U_g * A_g * DT_m \tag{5}$$

where U is the overall heat transfer coefficient and A is the heat transfer surface area (the subscripts w and g refer to water and gas sides, respectively). These quantities depend on the geometry of the heat exchanger as detailed in the following.

As described earlier, the process of designing the heat exchanger that was followed in this study was to first choose a set of values for the plausible physical characteristics of the AHX, calculate the associated value of ($\dot{Q}_{AHX}$), consider the difference between ($\dot{Q}_{AHX}$) that given by the LMTD method and ($\dot{Q}_p$) (given by DeltaEC), and to adjust the characteristics of the AHX until ($\dot{Q}_{AHX}=\dot{Q}_p$). The overall heat transfer coefficient is as follows:

$$\frac{1}{U_w*A_w} = \frac{1}{U_g*A_g} = \frac{1}{h_w*A_w} + \frac{1}{h_g*A_g*\eta_g} + \frac{ln(\frac{d_o}{d_i})}{2*\pi*L*k_c} + \frac{R_f''}{A_w} \tag{6}$$

where, h is the heat transfer coefficient on the water or gas side (the subscripts w and g refer to water and gas sides, respectively), η_g is the heat transfer surface area efficiency on the gas side, L is the total length of the tubes, (d_i) and (d_o) are respectively the inner and outer water tubes diameters, and R_f'' is the fouling coefficient.

The heat transfer coefficient on water side (h_w) for turbulent flow (i.e. $Re_{di} > 4000$) is given by [31]

$$h_w = 0.0243 * \frac{k_w}{d_i} * Re_{di}^{4/5} * Pr^{0.4} \tag{7}$$

where k_w is the thermal conductivity of the water, Re_{di} is Reynolds number based on the water tube internal diameter d_i and Pr is Prandtl number.

The heat transfer coefficient on gas side can be estimated as follows [32]:

$$h_g = \frac{k_g}{\sqrt{2}*\delta_k} \tag{8}$$

The efficiency of the heat transfer surface area (η_g) can be estimated as [29]

$$\eta_g = 1 - \frac{A_f}{A_g}(1 - \eta_f) \tag{9}$$

where A_f is the total surface area of the fins and η_f is the fin efficieny which is estimated to be about 97% for the current configuration [33]. Finally, the fouling factor (R_f'') during the induction period has a range from 0 to 0.0002 $m^2 K/W$ [29].

Based on the above set of equations, the value of the actual heat transfer rate ($\dot{Q}_{AHX}$) can be calculated. The different design parameters (e.g. water flow rate, fin thickness, fin spacing... etc.) can then be adjusted so that the actual heat transfer rate ($\dot{Q}_{AHX}$) becomes similar to the DeltaEC predicted heat transfer rate ($\dot{Q}_p$). In our device, this process suggested choosing the following characteristics for the AHX: the water tubes have an inner diameter (d_i) of 4 *mm* and hydraulic outer diameter (d_o) of 8 *mm*. The peripheral channel has a rectangular cross section 5.6 *mm* x 8.6 *mm* (see the yellow dashed lines in Figure 2b). Each of the 190 fins has a thickness of 1 *mm* and the fin spacing is 1.5 *mm*.

2.2.2. Design of the Cold Heat Exchanger (CHX)

In order to estimate the cooling capacity of the thermoacoustic refrigerator, the classical cold heat exchanger load from a delivered working fluid is replaced by electrical heaters. These

electrical heaters impose a controllable thermal load and, at thermal equilibrium, the oscillating cold gas flow balances this thermal load. When thermal equilibrium between the supplied and removed heats is achieved, the gas temperature is constant. Hence, the cooling capacity can be estimated for a certain gas temperature. In order to enforce a given gas temperature, an electrical circuit is used to control the temperature measured at the interface between the regenerator and the cold heat exchanger (T8, see Figure 1d) by regulating the amount of heat supplied via the heaters.

As shown in Figure 3, the cold heat exchanger consists of a 3D printed aluminum frame with a diameter of 140 mm and a length of 7 mm. As in the case of ambient heat exchanger, the cold heat exchanger is composed of a set of tubes and fins, but here the tubes are sized to fit the electrical cartridge heaters. Six cartridge heaters (Omega, model: HDC19107) are inserted in the tubes (diameter 3.6 mm). Each heater has an outer diameter of 3.2 mm, an electrical resistance of 144 Ω, and can deliver up to 100 W. In order to achieve a better thermal contact between the outer surface of the heaters and the tubes in the metal frame, a thermal conductive paste is used. The ability of the cold heat exchanger to impose the required amount of heat load on the oscillating gas flow is evaluated following the same method as described in the AHX section.
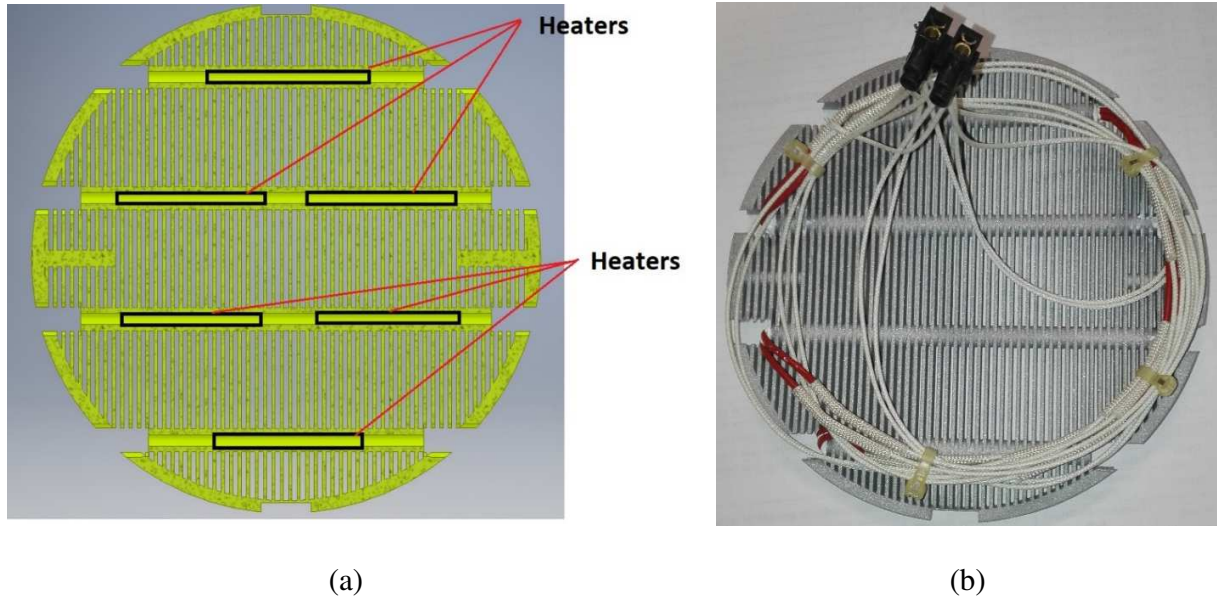
<div align="center">(a)   (b)</div>

Figure 3: (a) Schematic showing the internal design of the cold heat exchanger and (b) Photograph of the cold heat exchanger

2.3. Instrumentations and control systems

The characterization of the performance of the refrigerator requires measurements of several quantities such as temperatures, dynamic pressures at different locations of the system, and displacement of the piston of the acoustic driver. Figure 1d shows a description of the instrumentation used for these measurements.

Nineteen type-K thermocouples with a diameter of 0.5 *mm* are used to measure the temperature at different locations in the refrigerator. Three high-pressure feedthroughs are set at different locations in the refrigerator to pass the signals from the thermocouples while ensuring the sealing of the gas inside the machine. The signals of the thermocouples are connected to a data acquisition card (DAQ) (National Instruments, Model: NI9213). Three thermocouples are used to measure the temperature along the centerline of the regenerator: one at the cold side, one at the center of the regenerator, and one at the ambient side. These thermocouples give access to the

axial temperature profile within the regenerator, and can provide evidence of the presence of non-linear phenomena. Six other thermocouples are placed equidistant on the inside wall of the regenerator canister, three on the lower wall and the other three on the upper wall. These measurements allow detection of radial variations of the temperature. Such variations may produce natural convection effects [34]. The thermocouples were placed between the meshes of the regenerator that are compressed inside the canister to make sure that there is a good thermal contact between the tips of the thermocouples and the regenerator meshes. As the hydraulic radius of the mesh is much smaller than the thermal penetration depth, the gas and the solid temperatures are the same.

Tips of thermocouples

Figure 4: Photographs show the assembly of the meshes and the thermocouples inside the regenerator.

On each face of each heat exchangers, three thermocouples, radially distributed as the ones in the regenerator, are used to characterize the heat transferred by the exchangers. Three other thermocouples are positioned at different locations inside the driver's pressure vessel and one other fixed to the loudspeaker to make sure that the temperatures will not exceed the permitted operating temperature of these devices. Two Resistance Temperature Detectors (Newport Omega PT100 – 1/10 din) with high accuracy (±0.05 °C at 25 °C) are used to measure the inlet and

outlet temperatures of the water stream supplying the ambient heat exchanger. Together with the measurement of the water flow rate by a digital paddle wheel flow meter (Aalborg, model: PWE4), these measurements give access to the rate of heat delivered to the water. During the operation of the machine, the water flow rate is regulated so that the value of Reynolds number inside the tubes becomes higher than 4000 and hence equation (7) is always valid.

In order to control the temperature of the cold heat exchanger surface, a proportional-integral-differential temperature controller is used to keep the measured temperature (T8) at the set value.

Four high-precision dynamic pressure sensors (PCB Piezotronics, model: 113B28) are distributed at different locations in the device to monitor the dynamic pressures (Figure 1d).

An accelerometer (Viaxys, model: KS-91C) is used to monitor the movement of the driver piston. The signal of the accelerometer is connected to a DAQ (National Instruments, model: NI9234). The value of the acceleration is converted to a displacement via the operating frequency.

Two static pressure sensors (Endress & Hauser, model: Cerabar PMP21) are installed on each side of the machine and connected to the DAQ (model: NI9234). In order to prevent excessive piston displacement due to different static pressures across the electroacoustic source, an alarm sounds as soon as the measured static pressure difference exceeds 0.2 *bar*. This insures that the piston does not deviate more than 2 *mm* from its rest position.

The dynamic movement of the acoustic driver is protected by several control systems and sensors. Two diodes connected in parallel with the acoustic driver are used to limit the driver input voltage to 200 *Vrms*. Also, a 16 *Arms* fuse protects the driver against high currents. Moreover, the accelerometer signal is used to check that the piston displacement does not exceed

10 *mm* in amplitude; for larger amplitudes, an alarm is triggered. For immediate action, micro-limit-switches are used. Those are installed on each side of the piston at distances of 10 and 11 *mm*. If the piston touches any switch, the input electric signal is interrupted via a normally-closed mechanical relay. To cope with the potentially long response time of this mechanical relay, a low-resistance high-power resistor is connected in parallel with the acoustic driver via a normally-open solid-state relay so as to decrease the input signal as soon as the piston touches any switch.

2.4. Operating procedure and experimental conditions

The system is filled with a helium-argon mixture (70% He and 30% Ar volume basis) at a static mean pressure of 40 *bar*. A set of experiments are performed for different values of the piston displacement amplitude (X_p), cold side temperature (T8), relative phase between the acoustic driver (*AD*) and the loudspeaker (*LS*) voltages ($\emptyset_r = \emptyset_{AD} - \emptyset_{LS}$), and the drive ratio (*Dr*) (i.e. the ratio of the dynamic pressure amplitude at the location DPS4 (see Figure 1d) and the static pressure). As stated by [35], the maximum acoustic power delivered by an acoustic driver is achieved when both mechanical and the electrical resonance are coincident. Accordingly, the working frequency, for all experiments, is chosen to ensure that the driver operates at its mechanical resonance frequency (i.e. the phase between the piston velocity and the current applied to the driver is zero). In our system, the driver mechanical resonance frequency is very close to its electrical resonance frequency (i.e. the phase between the voltage and the current applied to the acoustic driver is zero), because the value of the inductance of the acoustic source is small (31.7 *mH*). Hence, the working frequency was chosen by setting the phase between the piston velocity and the current applied to the driver to zero and no additional capacitance was needed to reach electrical resonance. The value of the working frequency for all experiments was

set to be 47 Hz. It was determined that the amplitude of the loudspeaker input signal is not a critical parameter; therefore, it was not modified during the set of experiments. On the other hand, the relative phase between the two electroacoustic components is an important parameter that has to be chosen carefully.

Table 1 summarizes the different operating conditions. Two definitions of COP are used. First, the total coefficient-of-performance (COP_{Total}) represents the ratio between the cooling capacity and the input electric power to the acoustic source and the loudspeaker. The input electric powers are calculated via measuring the input voltage and current to the acoustic source and the loudspeaker. Second, the thermoacoustic coefficient-of-performance (COP_{TA}) represents the ratio between the cooling capacity and the acoustic power generated by the acoustic source. The acoustic power is estimated by the dynamic pressure measurement and the piston displacement measurement.

Experiments 1 to 4 correspond to the lower piston displacement amplitude $X_p = 5\ mm$, whereas Experiments 5 to 8 correspond to $X_p = 7\ mm$. Experiments 9 to 18 correspond to the limit amplitude $X_p = 8.5\ mm$ that is, 85% of the maximum allowable displacement. Experiments 13 to 18 were devoted to investigate the influence of the relative phase $\emptyset_r = \emptyset_{AD} - \emptyset_{LS}$.

For a given group of experiments, the prescribed cold temperature $T_c = T_8$ is set to a given value. Then the resulting hot side temperature $T_h = T_{14}$ and the actual cooling capacity of the refrigerator ($\dot{Q}_{CHX}$), which equals the heat supplied to the system by the electrical heaters, are measured. Experiments 4, 8, and 12 correspond to similar cold temperature ($T_c = 13\ °C$) and different acoustic amplitudes; other groups of similar cold temperature are Experiments 3, 7, and 11 for which $T_c = 8.5\ °C$ and Experiments 2, 6, 10 and 13 to 18 for which $T_c \approx 3.4\ °C$.

Exp#	X_p (mm)	$\emptyset_r$ (degrees)	T_c (^{O}C)	T_h (^{O}C)	$\dot{Q}_{CHX}$ (W)	COP_{TA}	COP_{Total}	Dr (%)
1	5	-60	-11.5	34.5	0	0	0	2.1
2	5	-60	4	36	125	2.7	1.5	2.1
3	5	-60	8.5	36	135.5	3.1	1.62	2.1
4	5	-60	13	36	162.5	4.0	1.92	2.1
5	7	-60	-13.8	39.6	0	0	0	2.9
6	7	-60	3.6	43.5	181	1.9	1.32	2.9
7	7	-60	8.5	43.5	218	2.4	1.45	2.9
8	7	-60	13.3	43.5	249	2.9	1.89	2.9
9	8.5	-60	-11.6	46.8	0	0	0	3.6
10	8.5	-60	2.5	45.8	170	1.3	0.85	3.6
11	8.5	-60	8.5	46	245	1.9	1.24	3.6
12	8.5	-60	13.3	47.2	290	2.3	1.5	3.6
13	8.5	0	2.7	52.3	165	1.25	0.8	3.6
14	8.5	-45	2.5	46.4	173	1.2	0.85	3.6
15	8.5	-90	2.6	45	143	1.06	0.73	3.6
16	8.5	-120	3	42.9	102	0.83	0.54	3.6
17	8.5	-150	4.1	44.2	75	0.7	0.42	3.6

23

18	8.5	-180	3.6	43.7	22	0.24	0.13	3.6

Table 1: The operating conditions of the experiments

3. RESULTS AND DISCUSSION

3.1. An overview of performance parameters

In this section, the calculated and measured performances of the refrigerator are presented for different acoustic levels and different prescribed cold heat exchanger temperatures, when the phase difference between the driver and the speaker is fixed. Results of Experiments 1 to 4 corresponding to a low piston displacement amplitude, Experiments 5 to 8 corresponding to a medium amplitude, and Experiments 9 to 18 corresponding to a large amplitude are then compared to results of calculation by DeltaEC. For the simulations, the cold and the hot temperatures and the piston displacement are set as targets; therefore, calculated and measured temperature difference are equal and the software converges to values of other parameters ($\dot{Q}_{CHX}$, $\dot{Q}_{AHX}$ and COP) to hit these targets. It is worthwhile to remember that the cooling capacity of the refrigerator ($\dot{Q}_{CHX}$) equals the heat rate supplied to the electrical heaters. In addition, the experimental heat rejected in the AHX ($\dot{Q}_{AHX}$) is calculated based on the measured difference between the outlet and inlet water temperatures and water flow-rate.

Figure 5 shows the evolution of experimental and calculated $\dot{Q}_{CHX}$, $\dot{Q}_{AHX}$, and COP$_{TA}$ with the piston displacement for different cold heat exchanger temperatures. Results of experiments and DeltaEC calculations are fairly close. As expected, the higher the acoustic amplitude, the higher the thermoacoustic effect, as shown by the increase of $\dot{Q}_{CHX}$ and $\dot{Q}_{AHX}$ when the piston displacement amplitude is increased. It should be noted that there is a little decrease in the experimental value of $\dot{Q}_{CHX}$ (see Figure 5a) when the piston displacement amplitude is increased from 7 mm to 8.5 mm at $T_C \approx 3.4$ °C. This decrease is mainly due to the small decrease (about 1

24

^{O}C) in cold side temperature at the piston displacement amplitude of 8.5 mm (i.e. the actual cold side temperature was 2.5 ^{O}C at piston displacement amplitude of 8.5 mm compared to 3.7 ^{O}C at piston displacement of 7 mm). As shown in Figure 5c, it was observed that both experimental and calculated COP$_{TA}$ slightly decrease as the piston displacement amplitude is increased. The measured slope of the decrease is steeper than the predicted one. This discrepancy can be attributed to an increase in non-linear losses, such as streaming and turbulence generation, that are not included in the calculation and that diminish the performance of thermoacoustic devices. In section 3.4. the origins of these discrepancies will be further discussed.

The temperature difference against which any refrigeration system can pump the heat is an important factor in qualifying the refrigeration system. Hence, the temperatures vs. axial distance along the refrigerator are plotted (Figure 5d) for different cases. It was observed that the temperature difference increases with the increase of the piston displacement amplitude; this indicates that when the acoustic amplitude is increased, the refrigerator can pump more heat across higher temperature difference. In addition, increasing the prescribed temperature at the CHX results in increasing the temperature difference over which the refrigerator works.
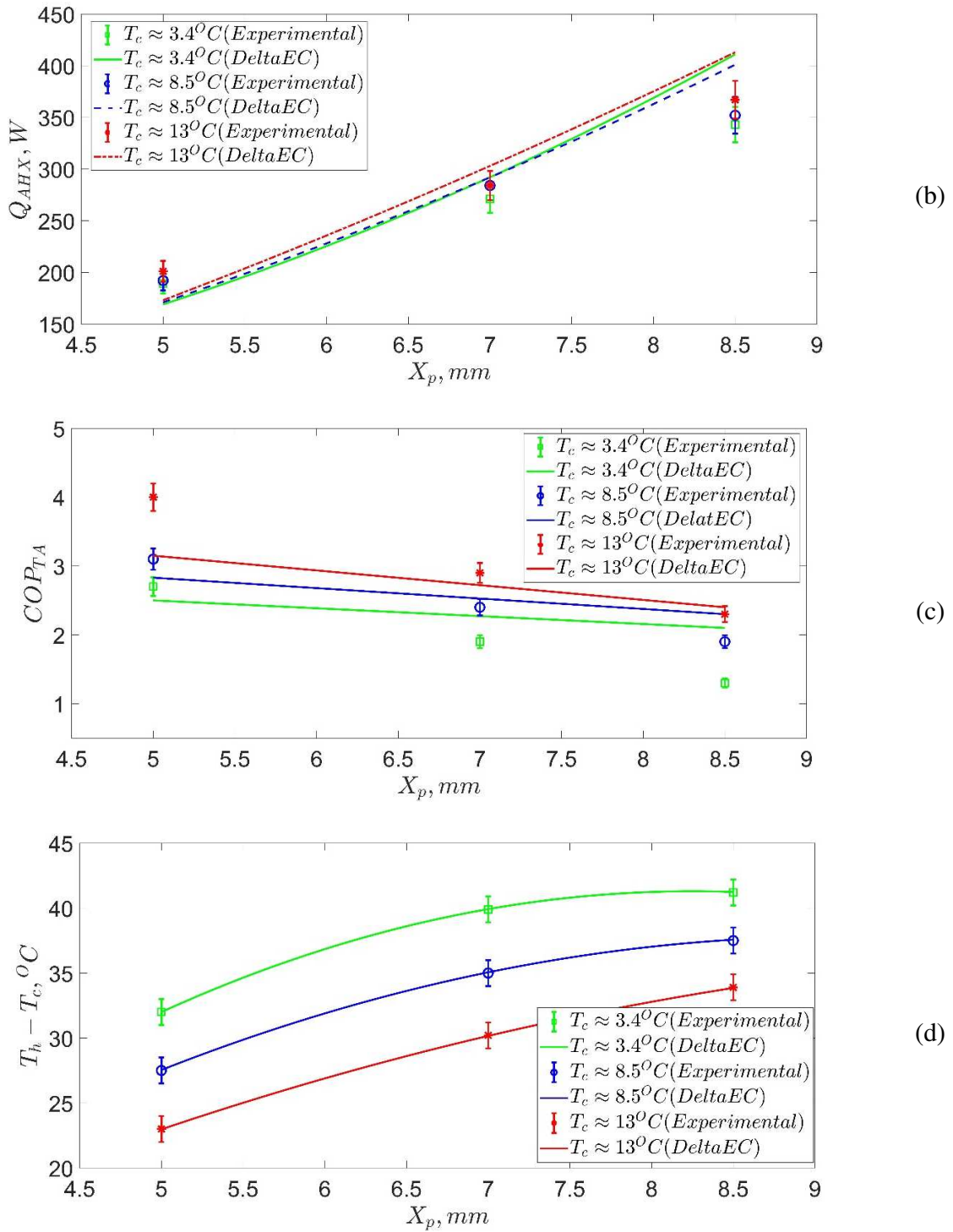

(a)

(b)

(c)

(d)
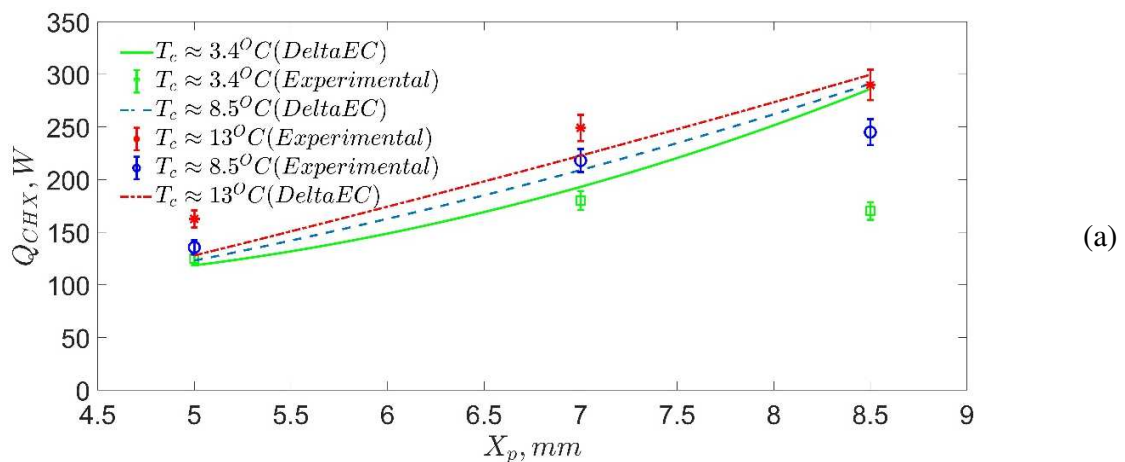
Figure 5: The effect of the piston displacement amplitude on (a) The cooling capacity, (b) The

heat rejected in the AHX, (c) The thermoacoustic coefficient-of-performance , (d) The

26

temperature difference across the regenerator for three different cold side temperatures and

phase difference between the driver and speaker of -60 degrees

In order to compare the performance of the present device to other thermoacoustic refrigerators, Table 2 shows the measured performance parameters at the design point corresponding to Experiment 12 together with the performance parameters of three other electrically driven thermoacoustic refrigerators as given by [24]. The power density is one of the important parameters that describe the compactness of the device. The power density (ρ_P) is calculated as follows:

$$\rho_P = \frac{\dot{Q}_{CHX}(T_h - T_c)}{V\, T_c} \tag{10}$$

The volume (V) used for this calculation represents the external volume of each device, much larger than the fluid volume inside the refrigerators. It should be noted that all the devices listed in Table 2 are research prototypes, that are designed to include extensive measurement systems and whose total volume is far from being as optimized as it is for commercial devices. The first two devices, TRITON and SETAC [36], use the resonance of a waveguide and were not designed to reach compactness, whereas the third device aimed at compactness. Table 2 shows that the new architecture proposed here achieves higher power density compared to the earlier devices.

Device	$\dot{Q}_{CHX}$ (W)	V (L)	$T_h - T_c$ (K)	T_c (K)	ρ_P (W/L)
TRITON	10^4	1000	17	281	0.6
SETAC	294	47	37	276	0.6
Ben & Jerry's	125	24	60	248	1.26
Current device	290	24	34	286	1.43

Table 2: Normalized power density of four thermoacoustic refrigerators, the last two being

compact devices.

3.2. The effect of the phase shift on the performance

In this section, the quest for optimal phasing between the electroacoustic components is discussed. For this purpose, the results of Experiments 10 and 13 - 18 corresponding to the same driver amplitude and same cold temperature, but different phases between the electroacoustic components, are compared to DeltaEC calculations in Figure 6. Results for $\dot{Q}_{CHX}$ and $\dot{Q}_{AHX}$ (Figure 6 (a) and (b)) show that the calculations predict an optimal phase between the two electroacoustic components of about -60 degrees. The experimental results show that the cooling capacity ($\dot{Q}_{CHX}$) also peaks at phase difference of -50 degrees (see Figure 6a). For this large acoustic amplitude, the experimental heat pumped is smaller than the predicted one for the same reasons discussed in the previous section. The experimental results of the heat rejected by the AHX shows a trend similar to the calculated results (see Figure 6b). The largest thermoacoustic effect was observed with the phase difference of around -60 degree in both the experiment and the DeltaEC calculations.
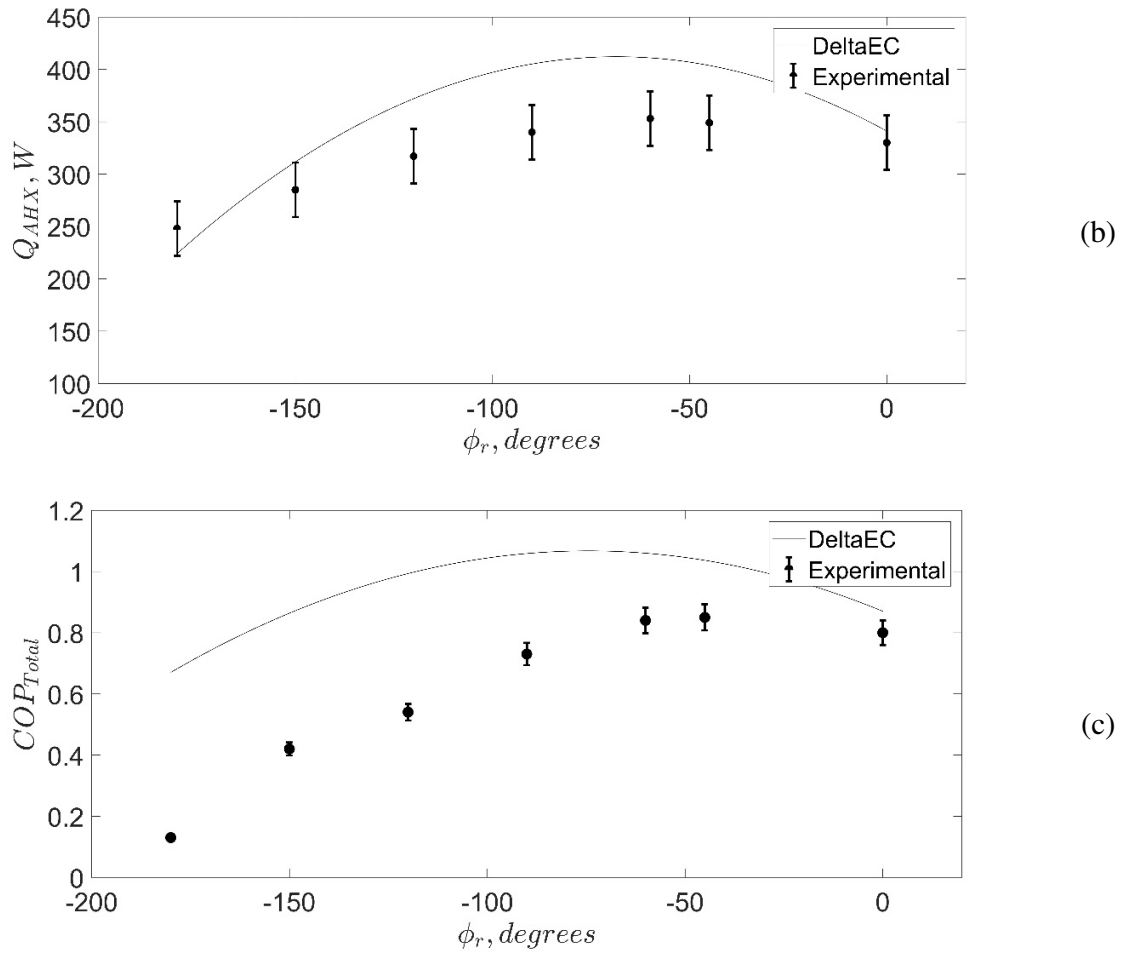

(a)

28

(b)

(c)
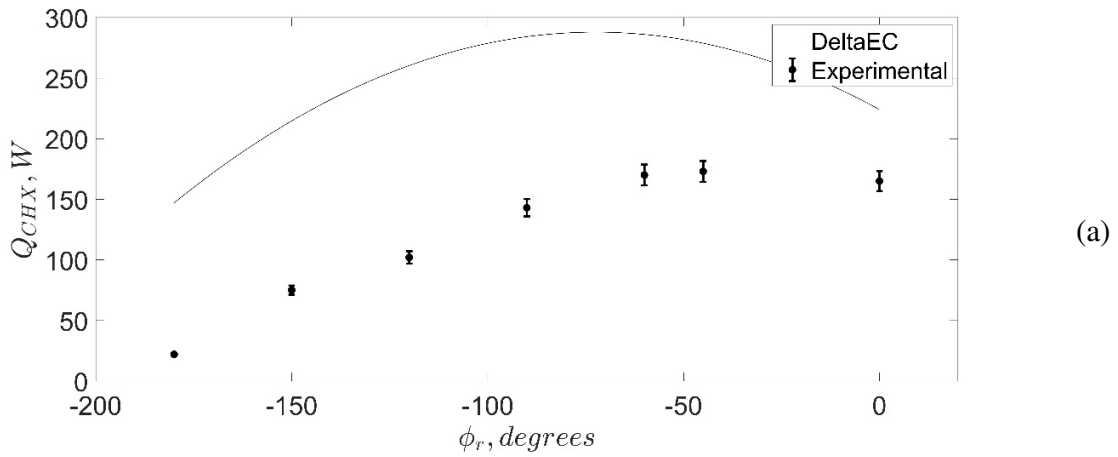
Figure 6: The effect of phase difference on (a) The cooling capacity, (b) The heat rejected in

the AHX, (c) The total coefficient-of-performance for cold side temperature of 3.4 ^{O}C and

piston displacement amplitude of 8.5 *mm*

3.3. Temperature distributions in the regenerator

The previous comparisons between experimental and calculated results show that the model can

predict the overall performance of the device. However, some discrepancies are observed.

Hence, exploring the available measurements may provide explanations for these discrepancies.

The axial temperature distributions at the middle plane of the regenerator for different

experimental conditions are plotted in Figure 7. As shown, the measured axial temperature

distributions are strongly non-linear. Also, for all experiments, the minimum temperature is achieved at the center of the regenerator, not at the cold side of the regenerator. For the different acoustic amplitudes, the overall shape of the temperature distribution follows a similar pattern. The temperature at the ambient heat exchanger remains constant for a given acoustic level because it is largely controlled by the water flowing through the exchanger. The temperature at the cold side follows the prescribed set value by the temperature regulation circuit, and thus changes with the experiment; the temperature at the center of the regenerator changes slightly with the particular experiment, but is always lower than the cold side temperature. On the other hand, the DeltaEC model always imposes a linear temperature distribution inside the regenerator. Note that the temperature measurements at both ends of the regenerator are used as input parameters to the DeltaEC model and hence, the measured and the model values of the temperatures at the ends of the regenerator are identical.

As shown in Figure 8, the vertical temperature distributions at the interface between the regenerator and the CHX are non-uniform and the maximum temperature is achieved at the upper positions. The vertical temperature gradient is much steeper when the heaters are turned-off (Experiments 1, 5 and 9) because, in these cases, the temperature is not forced to uniformity by the heaters at the CHX.

Lastly, the vertical temperature distributions at the interface between the regenerator and the AHX are plotted in Figure 9 for three different piston displacement amplitudes for different experimental conditions. For all experiments, the maximum temperature is observed at the middle plane. As shown in Figure 2, the thermocouples which measure the upper and the lower temperatures, are placed near the blocked part of the AHX (i.e. there are no openings for the

30

gas). Hence, the gas temperatures are highly affected by the water temperature in the peripheral

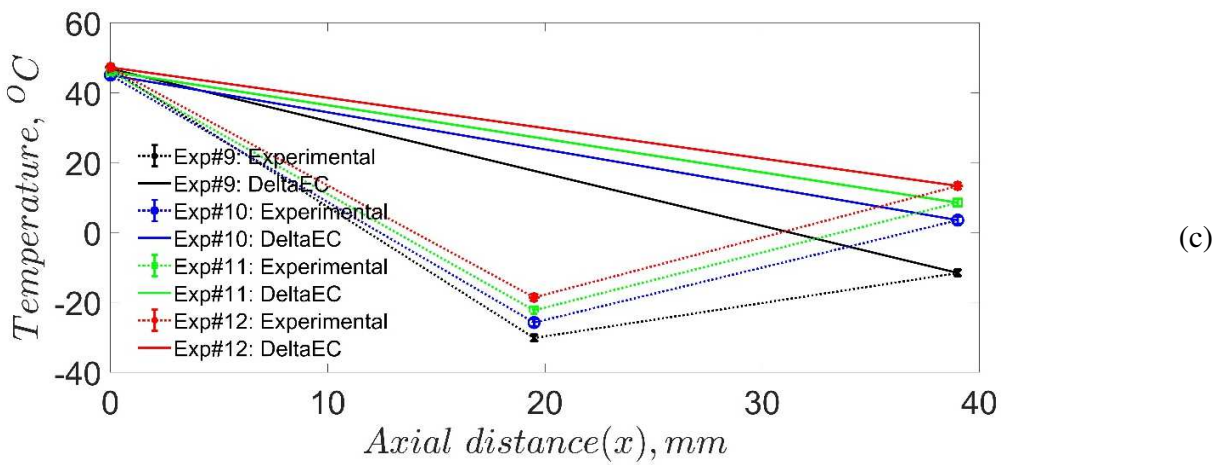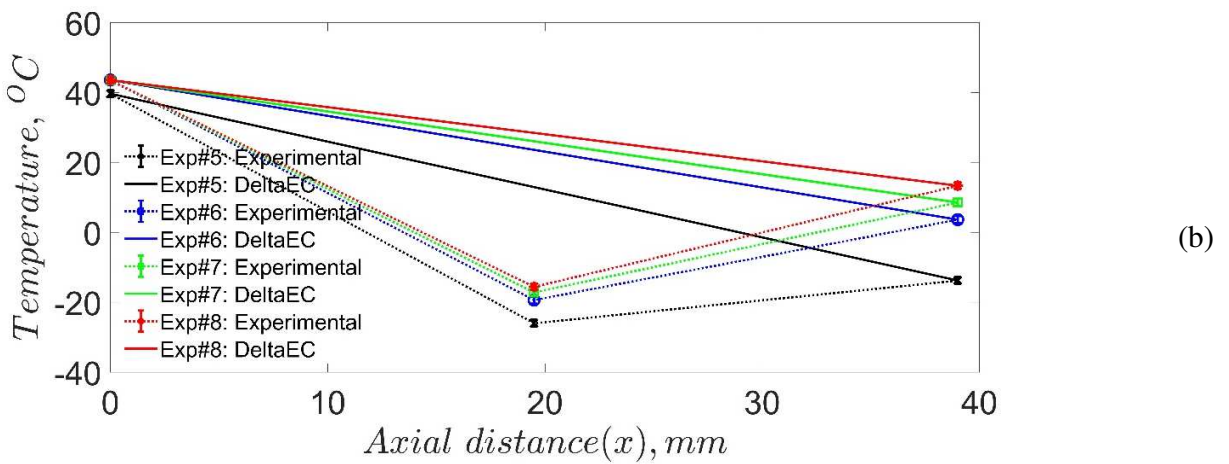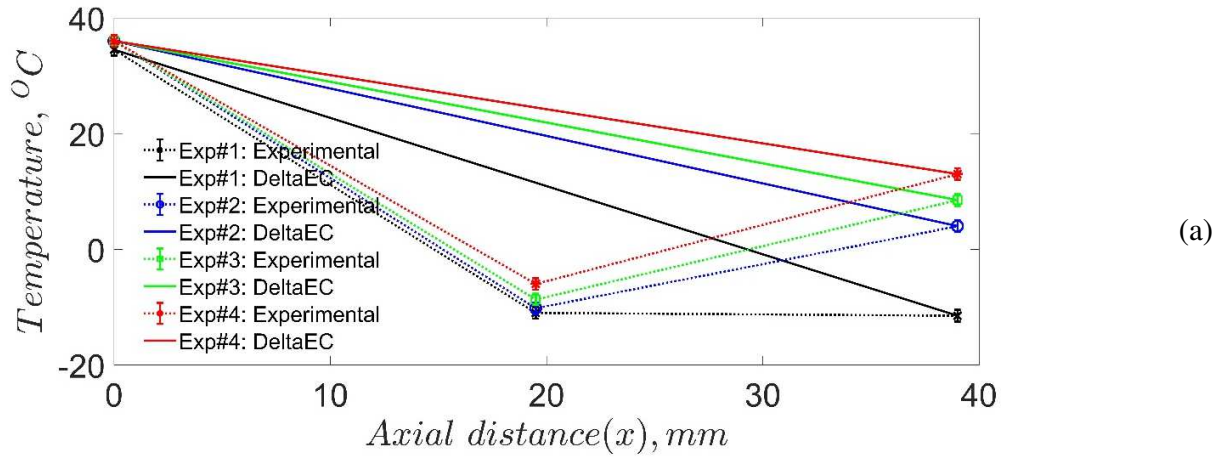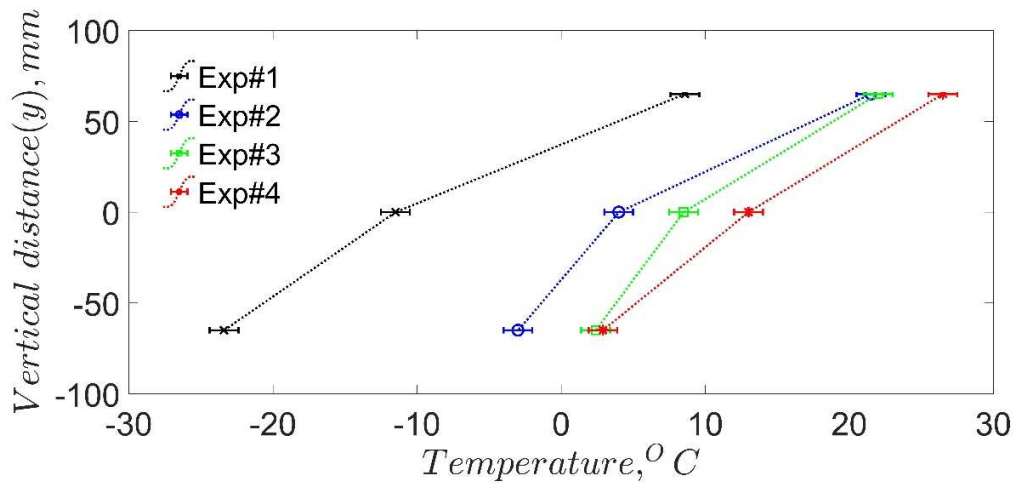channel. This explains the reduction in the measured temperatures at these positions.
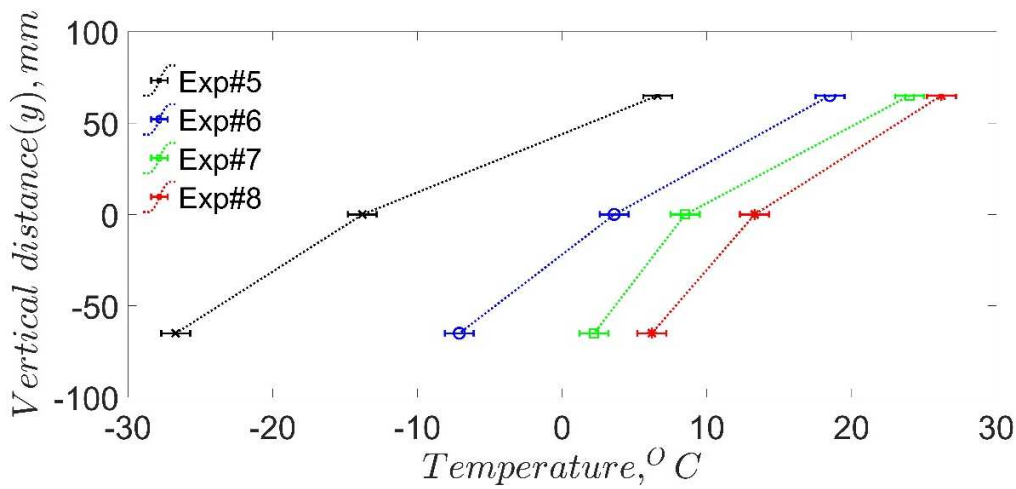
Figure 7: The axial temperature distribution in the middle plane of the regenerator at three different piston

displacement amplitudes (a) 5 *mm*, (b) 7 *mm* and (c) 8.5 *mm* for different experimental conditions

(a)

(b)

Figure 8: The vertical distribution of temperature at the interface between the regenerator and the CHX at three different piston displacement amplitudes (a) 5 *mm*, (b) 7 *mm* and (c) 8.5 *mm* for different experimental conditions
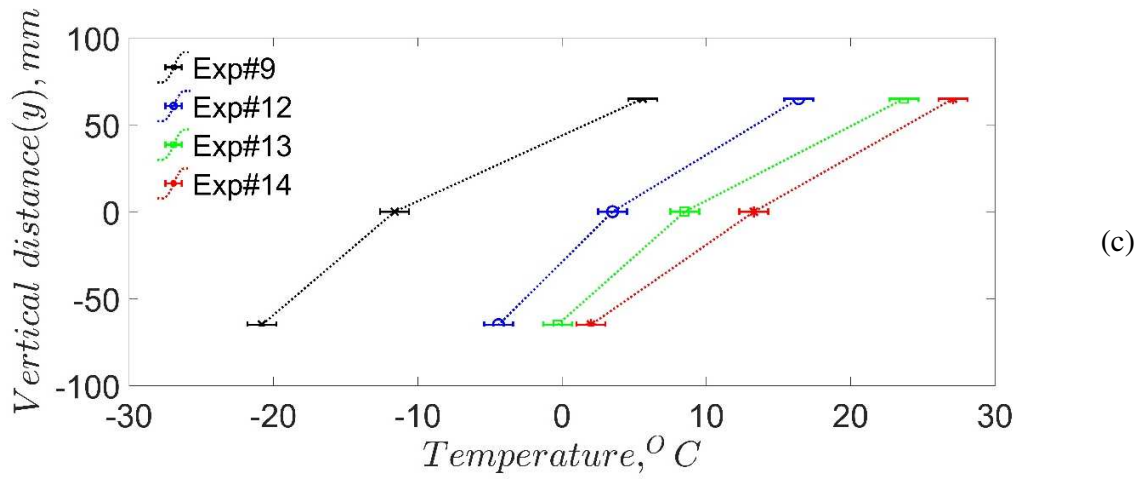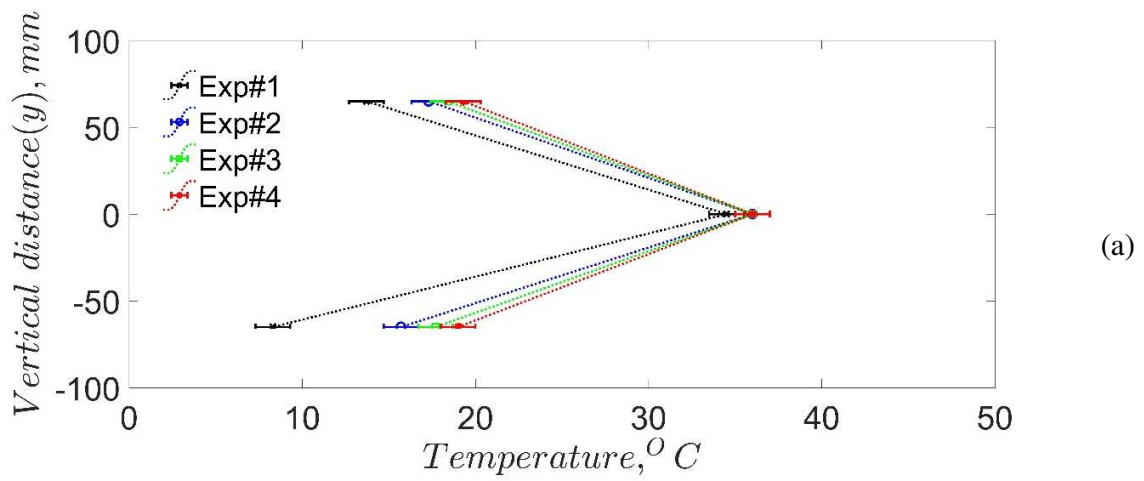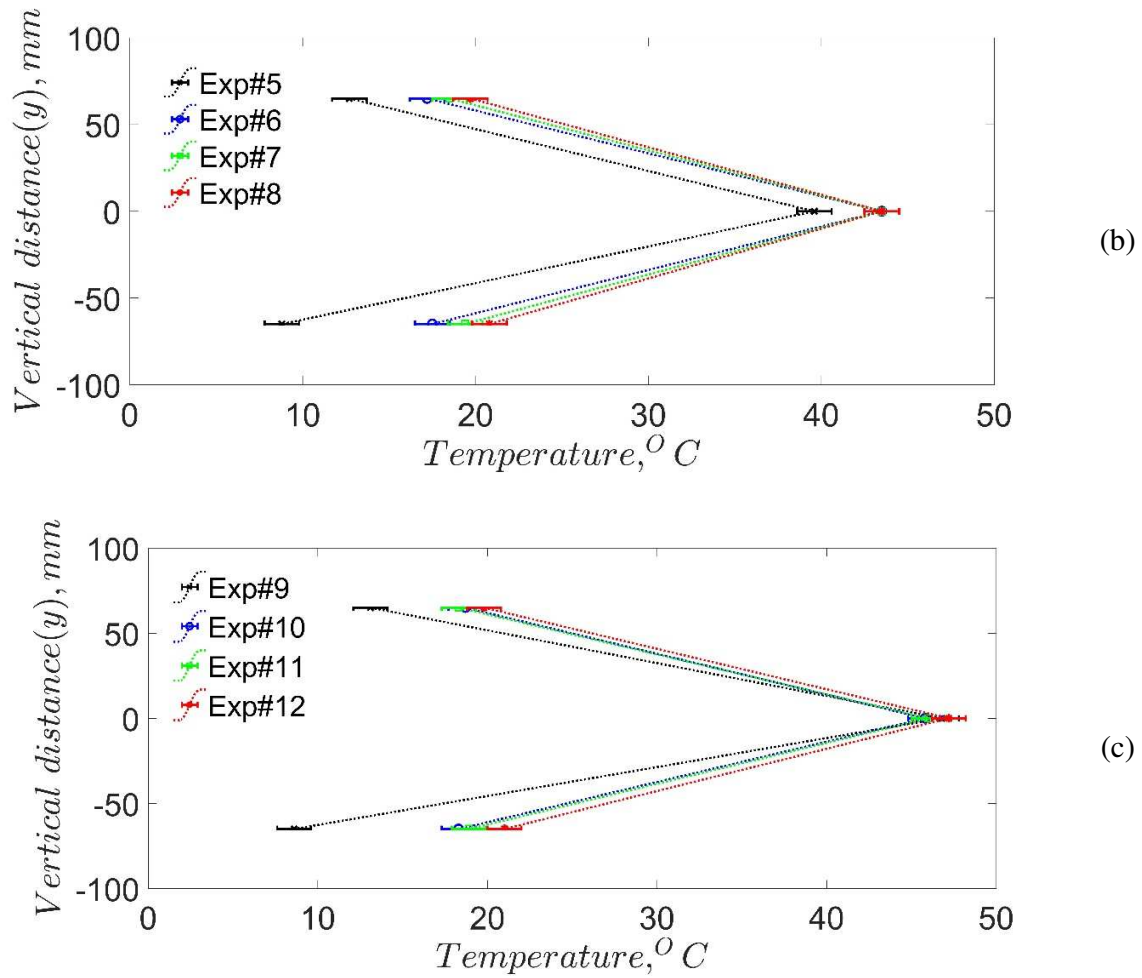
Figure 9: The vertical distribution of temperature at the interface between the regenerator and the AHX at three different piston displacement amplitudes (a) 5 *mm*, (b) 7 *mm* and (c) 8.5 *mm* for different experimental conditions

3.4. Beyond linear calculations

Figures 7 to 9 reveal non-linear effects that are not yet satisfactorily accounted for in the DeltaEC model. The objective of the present section is to discuss the possible sources of disagreement between the experimental and simulation results.

34

The observed increase in the temperature at the cold side of the regenerator (see Figure 7) can be discussed in terms of the thermal load imposed on the cold side. Theoretically, the thermal load on the cold side should be applied only by the CHX (i.e. electrical heaters). However, as stated above, the coldest point in the regenerator is never at the CHX interface, even for the experiments in which the heaters were turned-off (see Figure 7, Experiments 1, 5 and 9). Hence, it can be inferred that there are several nuisance sources for the thermal load on the cold side of the regenerator. The main, and desired, source is the heat added by the CHX (i.e. electrical heaters). In addition to that heat load, the heat generated by the acoustic driver can be transported towards the CHX either by the conduction in the metals, or by the convection via the oscillating gas, or by steady gas flow structures generated due to the area changes. It should be noted that two flow straighteners were installed (see Figure 1b) to eliminate the heat transported by large gas flow structures. Actually, this source of thermal load is a particularity of this device; the compactness brings the different elements of the device very close to each other. There are also heat leaks between the AHX and the CHX through the metal of the surrounding canister. However, the amount of heat leak is estimated to be few Watts at the maximum temperature difference. Actually, this amount of heat leak is lowered by reducing the wall thickness of the canister.

A suitable candidate for explaining the discrepancies between experimental and numerical results is natural convection. Figure 8 highlights the presence of a radial temperature gradient that can be due to natural convection. Similar radial temperature distribution was observed in [37] where the authors showed that this non-uniformity in the temperature distribution is due to the competition between the natural convection flow and Rayleigh streaming. However, in the current work, the vertical temperature gradient is much steeper than the temperature gradients

discussed in [37]. As stated in [34], the convection flow velocity at the extremity of the regenerator is proportional to the square-root of the regenerator radius. In the present device, the regenerator diameter is larger than in [34]; hence, the convection flow velocity is larger and this results in increasing the vertical temperature gradient.

Acoustic streaming is often pointed out as a good candidate for explaining the divergence between experiments and simulations in thermoacoustic devices. In the refrigerator under study here, Rayleigh and Gedeon streaming are not expected to develop along the thermoacoustic core due to the compactness of the device. Jet-driven streaming due to end-effects is more likely responsible for non-linearities. In Ramadan et al., [38], the characteristics of oscillating flow at the exit of a stack mesh grid regenerator were investigated. It is shown that the energy of fluctuations of the flow velocity at the exit of the regenerator greatly increases for Reynolds numbers above 50±20. The Reynolds number is defined as follows:

$$Re_{d_w} = \frac{U_r d_w}{\nu} \tag{11}$$

Where, U_r is the velocity amplitude of the oscillating gas at the exit of the regenerator, d_w is the wire diameter of mesh grid, and ν is the kinematic viscosity of the gas mixture. In the present device for a piston displacement amplitude of 7 mm, the Reynolds number (Re_{d_w}) at the exit of the regenerator is around 40. Hence, we can expect that the change of regime between low and high acoustic amplitude can lead to additional losses due to end-effects at the exit of the regenerator. This may be associated with the difference of slope between calculated and measured COP observed in Figure 5c. The effect of such phenomena on the thermal load at the heat exchanger and on the temperature distribution is far from being understood. However, we

can suspect that a change in the flow regime is associated with a change in the heat transfer process at the end of regenerator.

Another non-linear effect that can be observed in thermoacoustic devices is the energy cascade from the main oscillating frequency to upper harmonics due to non-linear propagation [39] [40]. In the particular device under study, due to its compactness, we expect that this cumulative effect would be less important than other non-linear effects discussed here.

Finally, the generation of turbulent flow, which represents an energy flow loss, should be considered. Few studies (e.g. [41] and [42]) have been focused on the transition to turbulence in oscillating flow in straight ducts. It was found that the relevant Reynolds number for transition to turbulence is defined as follows:

$$Re_\delta = \frac{U_o \delta_v}{\nu} \tag{12}$$

where, U_o is the velocity amplitude of the oscillating gas in the peripheral channel, δ_v is the viscous penetration depth ($\delta = \sqrt{\nu/\pi f}$), f is the frequency of the oscillations. The critical Reynolds number for transition to turbulence was found to be around 280 [41]. At a piston displacement amplitude of 8.5 mm, the velocity amplitude in the peripheral channel is about 4.7 m/s and hence the value of Reynolds number is about 365 that exceeds the critical Reynolds number. For a piston displacement amplitude of 7 mm, the value of the Reynolds number is about 290, close to the critical Reynold number. Such transition may be one of the reasons of the difference in experimental and numerical results observed in Figure 5. It should be noted that, here again, making great progresses in the understanding of the complex relation between flow dynamics and heat transfer is a necessity to discuss further the effects of such phenomena on the overall behavior of the device.

This discussion illustrates that research in thermoacoustic has reached a point where the available simulation tools can fairly predict the overall behavior of the devices. When looking more closely at this behavior, it appears that thermoacoustic devices continue to be rich sources of unsatisfactorily understood phenomena.

CONCLUSION

The design and testing of a new compact thermoacoustic refrigerator have been discussed. The refrigerator achieves a satisfactory normalized specific cooling capacity (the ratio between the cooling capacity and the volume of the device scaled by the temperature difference and the load temperature) of around 1.4 *W/L*. The achieved specific cooling capacity is higher than other existing thermoacoustic refrigerators. The good performance of the refrigerator besides its compactness is a leap towards improving the thermoacoustic technology to be used for several applications. A thermal design methodology for the heat exchangers has been proposed. A good agreement between the measured and the calculated quantities of the different heat rates is observed.

The performance indices, such as the heat rates, temperature difference, and the COP are measured under different experimental conditions. There is an overall good agreement between the measured quantities and DeltaEC predictions, which indicates that the model is reliable for the design of compact thermoacoustic systems. It was observed that the cooling capacity and the temperature difference increase with the increase of the piston displacement amplitude. However, the COP experiences a slight decrease with the increase in the piston displacement amplitude. The effects of the phase shift between the input voltages to the electroacoustic components on the performance indices have been investigated. It is found that the maximum measured cooling capacity is achieved at a phase shift of approximately -60 degrees. DeltaEC

predicts a maximum cooling capacity at the same phase shift. The axial and vertical temperature distributions inside the regenerator were measured. It is found that the axial temperature distribution in the middle plane of the regenerator is non-linear, which is different from the predicted temperature distribution by the DeltaEC model. The vertical temperature distribution shows large non-uniformity that suggests the existence of natural convection flow inside the refrigerator.

This further analysis of the results of measurements, together with their comparison to results of calculations, shows that although a fair choice of guesses and targets in the model allows its convergence through realistic overall performance compared to experiments, non-linear phenomena yield discrepancies between model and experience. A preliminary discussion of the different non-linear phenomena that can contribute to these discrepancies is proposed. Further research is needed to clearly understand the effects of these phenomena on the performance of thermoacoustic devices.

References

[1] B. H. Kang and H. Lee, "A Review of Recent Research on Automotive HVAC Systems for EVs," *International Journal of Air-Conditioning and Refrigeration,* vol. 25, no. 4, 2017.

[2] M. Bentrcia, M. Alshatewi and H. Omar, "Developments of vapor-compression systems for vehicle air-conditioning:A review," *Advances in Mechanical Engineering,* vol. 9, no. 8, 2017.

[3] Y. Lee and D. Jung, "A brief performance comparison of R1234yf and R134a in a bench tester for automobile applications," *Applied Thermal Engineering,* vol. 35, p. 240–242, 2012.

[4] J. K. Vaghela, "Comparative Evaluation of an Automobile Air - Conditioning System Using R134a and Its Alternative Refrigerants," *Energy Procedia,* vol. 109, pp. 153-160, 2017.

[5] J. S. Brown, S. F. Yana-Motta and P. A. Domanski, "Comparative analysis of an automotive air conditioning systems operating with CO2and R134," *International Journal of Refrigeration,* vol. 25, p. 19–32, 2002.

[6] L. Zoontjens, C. Howard, A. Zander and B. Cazzolato, "Feasibility Study of an Automotive Thermoacoustic Thermoacoustic Refrigerator," in *Proceedings of ACOUSTICS*, Busselton, Western Australia, 2005.

[7] H. Babaei and K. Siddiqui, "Design optimization of an automotive thermoacoustic air refrigeration system," *Acoustique Canadienne,* vol. 35, pp. 166 -167, 2007.

[8] R. Keolian, "Truck Thermoacoustic Generator and Chiller," U.S. Department of Energy-Office of Scientific and Technical Information, 2011.

[9] M. Karlsson, M. Åbom, M. Lalit and R. Glav, "A Note on the Applicability of Thermo-Acoustic Engines for Automotive Waste Heat Recovery," *SAE Int. J. Mater. Manf,* vol. 9, no. 2, 2016.

[10] P. C. Bansod and A. S. Raut, "Review on Thermoacoustic Refrigeration," *International Journal of Innovations in Engineering and Science,* vol. 2, no. 3, 2017.

[11] W. Dai, E. Luo, J. Hu and H. Ling, "A Heat-driven thermoacoustic cooler capable of reaching liquid nitrogen temperature," *Appl. Phys. Let.,* vol. 86, 2005.

[12] J. Wollan, G. Swift, S. Backhaus and D. Gardner, "Development of a thermoacoustic natural gas liquefier," in *AIChE New Orleans Meeting*, New Orleans, LA, 2002.

[13] S. Backhaus, E. Tward and M. Petach, "Traveling-wave thermoacoustic electric generator," *Appl. Phys. Let.,* vol. 85, no. 6, 2004.

[14] E. Luo, W. Dai, Y. Zhang and H. Ling, "Thermoacoustically driven refrigerator with double thermoacoustic Stirling cycles," *Appl. Phys. Let.,* vol. 88, no. 074102, 2006.

[15] O. Symko, E. Abdel-Rahman, Y. Kwon, M. Emmi and R. Behunin, "Design and development of high-frequency thermoacoustic engines for thermal management in microelectronics," *Microelectronics Journal ,* vol. 35, pp. 185-191, 2004.

[16] M. Tijani and S. Spoelstra, "Study of a coaxial thermoacoustic-Stirling cooler," *Cryogenics,* vol. 48, pp. 77-82, 2008.

[17] L. M. Zhang, J. Y. Hu, Z. H. Wu, E. C. Luo, J. Y. Xu and T. J. Bi, "A 1 kW-class multi-stage heat-driven thermoacoustic cryocooler system operating at liquefied natural gas temperature range," *Appl. Phys. Let,* vol. 107, no. 3, p. 033905, 2015.

[18]   L. K. Tartibu, "Developing more efficient travelling-wave thermo-acoustic refrigerators: A review," *Sustainable Energy Technologies and Assessments,* vol. 31, p. 102-114, 2019.

[19]   K. De Blok and A. T. Systemen, "Multi-stage traveling wave thermoacoustics in practice," in *19th Int. Congress Sound Vibration*, Vilnius, July 2012.

[20]   K. Luo, D. Sun, J. Zhang, Q. Shen and N. Zhang, "A multi-stage traveling-wave thermoacoustically-driven refrigeration system operating at liquefied natural gas temperature," in *IOP Conference Series: Materials Science and Engineering*, 2017.

[21]   M. Bassem, Y. Ueda and A. Akisawa, "Design and construction of a traveling wave thermoacoustic refrigerator," *Int. J. Refrig.,* vol. 34, no. 4, p. 1125–1131, 2011.

[22]   A. I. Abd El-Rahman, W. A. Abdelfattah, K. S. Abdelwahed, A. Salama, A. Rabie and A. Hamdy, "A compact standing-wave thermoacoustic refrigerator driven by a rotary drive mechanism," *Case Studies in Thermal Engineering,* vol. 21, p. 100708, 2020.

[23]   M. Poese, R. Keolian, R. Smith, E. Mitchell, C. Roberts and S. Garrett, "Trillium: A thermoacoustic-Stirling refrigerator implementation using an inline topology," in *Proceedings of the third international workshop on thermoacoustics*, Twente, Netherlands, 2015.

[24]   M. Poese, R. Smith, S. Garrett, R. van Gerwen and P. Gosselin, "Thermoacoustic refrigeration for ice cream sales," in *6th Gustav Lorentzen Natural Working Fluids*, Glasgow, UK, 2004.

[25]   G. Poignand, B. Lihoreau, P. Lotton, E. Gaviot , M. Bruneau and V. Gusev, "Optimal acoustic fields in compact thermoacoustic refrigerators," *Applied Acoustics,* vol. 68, p. 642–659, 2007.

[26]   G. Poignand, P. Lotton, G. Penelet and M. Bruneau, "Thermoacoustic, Small Cavity Excitation to Achieve Optimal Performance," *Acta Acustica united with Acustica,* vol. 97, p. 926 – 932, 2011.

[27]   G. Poignand, A. Podkovskiy, G. Penelet, P. Lotton and M. Bruneau, "Analysis of a Coaxial, Compact Thermoacoustic heat pump," *Acta Acust. United Ac.,* vol. 99, p. 898 – 904, 2013.

[28]   J. Clark, W. Ward and G. Swift, "Design environment for low-amplitude thermoacoustic energy conversion (DeltaEC)," *J. Acoust. Soc. Am.,* vol. 122, p. 3014, 2007.

[29]   W. M. Kays and A. L. London, Compact heat exchangers; a summary of basic heat transfer and flow friction design data, New York: McGraw-Hill, 1958.

[30]   C. Oko , E. Diemuodeke and M. Katsina, "Spreadsheet Add-in for Heat Exchanger Logarithmic Mean Temperature Difference Correction Factor," *International Journal of Computer Applications,* vol. 44, no. 5, pp. 24-30, 2012.

[31]   F. Incropera, Fundamentals of Heat and Mass Transfer, 2011.

[32]   A. Piccolo and G. Pistone, "Estimation of heat transfer coefficients in oscillating flows: The thermoacoustic case," *International Journal of Heat and Mass Transfer,* vol. 49, p. 1631–1642, 2006.

[33]   D. Taler and J. Taler, "Steady-state and transient heat transfer through fins of complex geometry," *Archives of thermodynamics,* vol. 35, no. 2, p. 117–133, 2014.

[O. Hireche, I. Ramadan, C. Weisman, H. Bailliet, Y. Fraigneau, D. Baltean-Carlès and

34] V. Daru, "Experimental and numerical investigation of natural convection flows in two horizontal thermoacoustic cavities," *International Journal of Heat and Mass Transfer,* vol. 149, 2020.

[35] D. Sun, K. Wang, X. Zhang, Y. Guo, Y. Xu and L. Qiu, "A traveling-wave thermoacoustic electric generator with a variable electric R-C load," *Applied Energy,* vol. 106, p. 377–382, 2013.

[36] S. L. Garrett, "High power thermoacoustic refrigerator". USA Patent US5647216A, 15 July 1997.

[37] I. Ramadan, H. Bailliet and J.-C. Valiere, "Experimental investigation of the influence of natural convection and end-effects on Rayleigh streaming in a thermoacoustic engine," *J. Acoust. Soc. Am.,* vol. 143, no. 1, 2018.

[38] I. Ramadan, H. Bailliet and J.-C. Valiere, "Experimental investigation of oscillating flow characteristics at the exit of a stacked mesh grid regenerator," *J. Acoust. Soc. Am.,* Accepted for publication on 3 January 2021.

[39] T. Biwa, K. Sobata, S. Otake and T. Yazaki, "Observation of thermoacoustic shock waves in a resonance tube," *J. Acoust. Soc. Am.,* vol. 136, no. 3, p. 965–968, 2014.

[40] C. Olivier, G. Penelet, G. Poignand, J. Gilbert and P. Lotton, "Weakly nonlinear propagation in thermoacoustic engines: a numerical study of higher harmonics generation up to the appearance of shock waves," *Acta Acust. United Ac.,* vol. 101, no. 5, p. 941–949, 2015.

[41] P. Merkli and H. Thomann, "Transition to turbulence in oscillating pipe flow," *Journal of fluid mechanics,* vol. 68, pp. 567-576, 1975.

[42] I. Reyt, H. Bailliet, E. Foucault and J. Valière, "Oscillating viscous boundary layer at high Reynolds number: Experiments and numerical calculations," *AIP Conference Proceedings,* vol. 1685.